Mesoporous indium tin oxide perovskite solar cells in bifacial configuration

Journal of Physics: Energy

PAPER

Mesoporous indium tin oxide perovskite solar cells in bifacial configuration

Maayan Sohmer, Shir Yudco and Lioz Etgar*

Institute of Chemistry, Casali Center for Applied Chemistry, The Hebrew University of Jerusalem, Jerusalem 91904, Israel
* Author to whom any correspondence should be addressed.

E-mail: lioz.etgar@mail.huji.ac.il

Keywords: perovskite, bifacial solar cell, impedance, ITO mesoporous

Supplementary material for this article is available online

OPEN ACCESS

RECEIVED
17 June 2022

REVISED
9 September 2022

ACCEPTED FOR PUBLICATION
28 September 2022

PUBLISHED
26 October 2022

Abstract

In this work, we present a fully printable mesoporous (mp) indium tin oxide (ITO) perovskite solar cell. The solar cell structure consists of triple-oxide screen-printed mp layers. In this structure, the perovskite does not form a separate layer but fills the pores of the triple-oxide structure. The perovskite is utilized as both a light harvester and a hole transporting material. One of the advantages of this solar cell structure is the transparent contact (mp ITO), which permits the use of this cell structure in a bifacial configuration without the need for additional layers or thinner counter electrodes. We performed photovoltaic (PV) measurements on both sides (i.e. ITO side and glass side), where the glass side shows 15.3% efficiency compared to 4.4% of the ITO side. Further study of the mechanism shows that the dominant mechanism when illuminating from the glass side is Shockley–Read–Hall recombination in the bulk, while illuminating from the ITO side shows recombination in multiple traps and inter-gap defect distribution, which explains the poor PV performance of the ITO side. Electrochemical impedance spectroscopy sheds more light on the resistance and capacitance. Finally, we demonstrate 18.3% efficiency in the bifacial configuration. This work presents a fully printable, large-scale suitable solar cell structure that can function in a bifacial configuration.

1. Introduction

In recent years, the research of renewable energy sources, specifically solar energy, has expanded in an attempt to reduce the dependence on coal-based energy. Different types of solar cells are investigated, such as organic solar cells, dye sensitized solar cells and perovskite solar cells (PSCs). PSCs have been breaking efficiency records, with the power conversion efficiency (PCE) increasing from 3.81% to 25.5% in a decade [1]. Metal lead halide perovskite has drawn interest, due to its suitable photovoltaic (PV) properties, such as tunable band gap, long diffusion length, low exciton binding energy and a high absorbance coefficient [2–6]. Standard PSCs are built on top of a transparent electrode, where the perovskite layer is placed between an electron transport layer (ETL) and a hole transport layer (HTL). The perovskite functions as the light harvester of the solar cell. Usually, a noble metal, such as gold or silver, is evaporated on top of the structure as a back contact. When light penetrates the transparent electrode and absorbs in the perovskite, the generated electron–hole pairs separate into the selective contacts. Unlike conventional monofacial solar cells, bifacial solar cells absorb photons from both the front and the back electrodes, resulting in enhanced power output. Bifacial solar cells are considered promising future PV technology, due to the reduced balance of system costs, improved efficiency and the option to implement them at different angles and in different directions [7]. Different PSC structures were studied as bifacial structures, but different adjustments were required, such as thinning the metal back electrode or adding an optical coupling layer [8–11].

Despite the impressive efficiency achieved, there are several obstacles in the up-scale of PSC technology. For example, different layers of PSCs can be fabricated using different techniques, including spin coating,

atomic layer deposition, spray deposition, high vacuum evaporation, etc. Some of these methods are not suitable for large-scale production, and some are power consuming [12]. Another possible fabrication method is screen printing, in which a mesh is used to transfer a paste of the material in a desired pattern to the substrate. Screen printing is very common in different industries and is suitable for mass production.

Our previous work demonstrates a unique structure, with triple-oxide screen-printed mesoporous (mp) layers. This structure is composed of a fully screen-printed inorganic scaffold and perovskite as the light-harvesting material, filling the pores of the triple-oxide structure. The perovskite, deposited from a solution and crystallized inside the mp structure, is utilized as both the light harvester and as the hole transporting material. The counter electrode, unlike the different PSC structures, is not a noble metal or carbon but a mp indium tin oxide (ITO) layer. This unique HTL-free structure has several advantages, such as enhanced stability and renewability compared to the other screen-printed structure with a carbon counter electrode [13]. In addition to a simple and scalable fabrication method, this solar cell structure is a good candidate for large-scale production.

In this work, we study and characterize the ITO-PSC structure from both directions (i.e. glass and ITO sides), taking advantage of the transparency of the mp ITO contact, as opposed to the conventional opaque back contacts. Optical characterizations, PV performance, external quantum efficiency (EQE) and impedance spectroscopy were used to study this solar cell structure and investigate its bifacial potential.

Finally, the ITO-PSC PV performance was measured in a bifacial configuration, achieving 18.3% efficiency. Double-illumination measurements demonstrate the potential of these solar cells as bifacial PV devices, opening the possibility for a scalable, printable solar cell without directional demands.

2. Results and discussion

The ITO-PSC configuration is based on a triple-oxide mp structure, as presented in figure 1(a). On top of a fluorine tin oxide (FTO) coated glass, mp TiO_2, mp ZrO_2 and mp ITO layers are screen printed. The thickness of the mp-TiO_2 is about 0.7 μm, which serves as the ETL. The thickness of the mp-ITO layer is about 5 μm, acting as the back contact of the cell. A 1 μm thick mp-ZrO_2 layer separates these two layers, to avoid direct contact between the anode and the cathode [14]. The layers of the solar cell can be observed in the cross-sectional image made by a focused ion beam (FIB), as presented in figure 1(b). The perovskite composition used in this work is mixed cation, mixed halide, $FA_{0.85}MA_{0.15}Pb(I_{0.85}Br_{0.15})_3$ (FA-formamidinium, MA-methylammonium).

The perovskite is deposited using a two-step deposition method, where the perovskite precursor solutions percolate through the mp structure, from the mp ITO through the mp TiO_2, and crystallize inside the pores. Figure 1(d) shows images of the cell from both sides. The black circle represents the perovskite inside the mp of the cell. Due to the difference in the energy levels (figure 1(c)) between the perovskite, the TiO_2 and the ITO, there is a preferred direction for electron and hole transport that results in a PV response following illumination of the solar cell.

As presented in table 1, the ITO-PSCs achieve an average efficiency of 13.7%, with an average current density of 24 mA cm^{-2} and an average open circuit voltage of 0.93 V. Figure 2(a) presents a stable power output and current density output over time, with the average PCE and J_{sc} maintaining the average values through 12 sequential measurements. The champion cell achieved PCE of 15.3%. Its J–V curve and EQE can be observed in figures 2(b) and (c), respectively. There is a very good agreement between the J_{sc} measured by the solar simulator and the integrated J_{sc}. As can be seen in figure 2(d), this perovskite composition absorbs through the entire visible spectrum to the near infra-red (IR) with 1.56 eV as an example, which is in agreement with current densities achieved for these cells [15].

In addition to the possibility to function as a solar cell, the ITO-based cell can also function as an LED. In order for the ITO-PSCs to function as LEDs, the positions of the energy levels are aligned under applied bias to achieve radiative recombination. In addition, it is required that the layers be as thin as possible, to minimize non-radiative recombination. Here, we performed EL measurements on the ITO-PSC, as presented in figures 2 (e) and (f). Surprisingly, despite the thickness of this structure (about 7 μm overall), an emission was detected with an applied bias of 5–19 V. Although the EL intensity is relatively low compared to conventional perovskite LEDs, the voltage range of the EL is relatively wide, indicating that this unique structure might have potential in more applications. Figure 2(f) presents EL spectra with a peak position at 800 nm.

2.1. Measurements of both sides

Unlike traditional PSC structures (e.g. planar and meso PSCs), the structure of ITO-PSCs does not include a metal contact that blocks the light from passing through it. Therefore, in backside illumination, the light is not reflected by metal contact and absorbed by the perovskite. Since the ITO has some transparency, it is

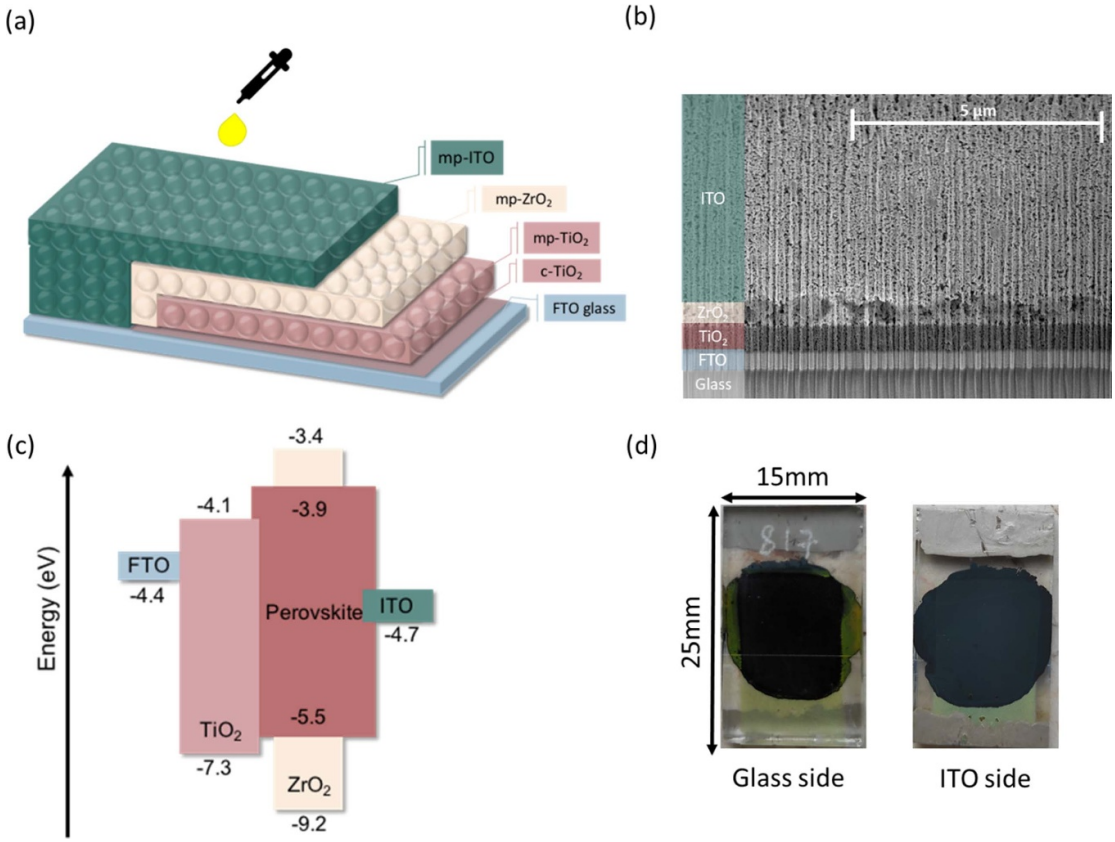

Figure 1. (a) FTO/mp-TiO_2/mp-ZrO_2/mp-ITO solar cell structure. $FA_{0.85}MA_{0.15}Pb(I_{0.85}Br_{0.15})_3$ perovskite precursor solution infiltrates into the mesoscopic structure. (b) Cross-sectional image of the structure using FIB. (c) Energy-level diagram of the different layers in the structure. Energy values were taken from [13]. (d) Images of the ITO-PSC from both sides.

Table 1. The champion and average (in brackets) PV parameters of the ITO-PSCs, when illuminating from the glass and the ITO sides.

Direction of illumination	V_{oc} (V)	J_{sc} (mA cm^{-2})	FF (%)	Eff (%)
Glass	1.00 (0.93 ± 0.05)	25.6 (24 ± 1)	59 (60 ± 3)	15.3 (13.7 ± 0.7)
ITO	0.87 (0.82 ± 0.06)	9.1 (7 ± 1)	56 (64 ± 3)	4.44 (3.4 ± 0.7)

possible to illuminate the cell from both sides, i.e. the ITO side and the glass side. Measuring the ITO-PSC from both sides can provide information regarding the charge transport process in this structure and can demonstrate the possibility of this cell structure functioning in a bifacial configuration.

Current voltage (I–V) measurement was performed from the ITO side. As expected, illumination from the ITO side results in significantly lower PV performance, compared to illumination from the glass side (table 1). The main decrease can be observed in the short-circuit current (J_{sc}) and the efficiency, while the average fill factor (FF) is slightly higher for the glass-side measurement. The open-circuit voltage (V_{oc}) slightly decreased (by 12%).

In order to characterize the mechanism of ITO-PSC when illuminated from both sides, the J_{sc} and V_{oc} were measured at different light intensities, from 10−100 mW cm^{-2} (equivalent to 0.1–1 sun illumination). The J_{sc} is proportional to the light intensity according to $J \propto I^{\alpha}$, when the value of α gives information about the part of the electron recombination in the cell [16]. The dependence of the current on the light intensity is presented in figure 3(a), for glass- and ITO-side illumination. For illumination from the glass side, the value of α is 0.95, which indicates that the ITO-PSC structure has no space-charge limit, and most of the excited electrons are injected into the electrode before recombination. When illuminating from the ITO side, the value of α is 0.7 (figure 3(a)). In this case, not all the electrons reach the electrode, which suggests enhanced recombination [17]. Measuring the photoluminescence (PL) from both sides of the cell supports this assumption, as can be seen in figure 3(b). When measured from the glass side, the quenching is more significant than when measured from the ITO side, indicating reduced radiative recombination.

More information about the recombination processes in the cell can be learned from the dependence of V_{oc} on the light intensity (figure 3(c)).

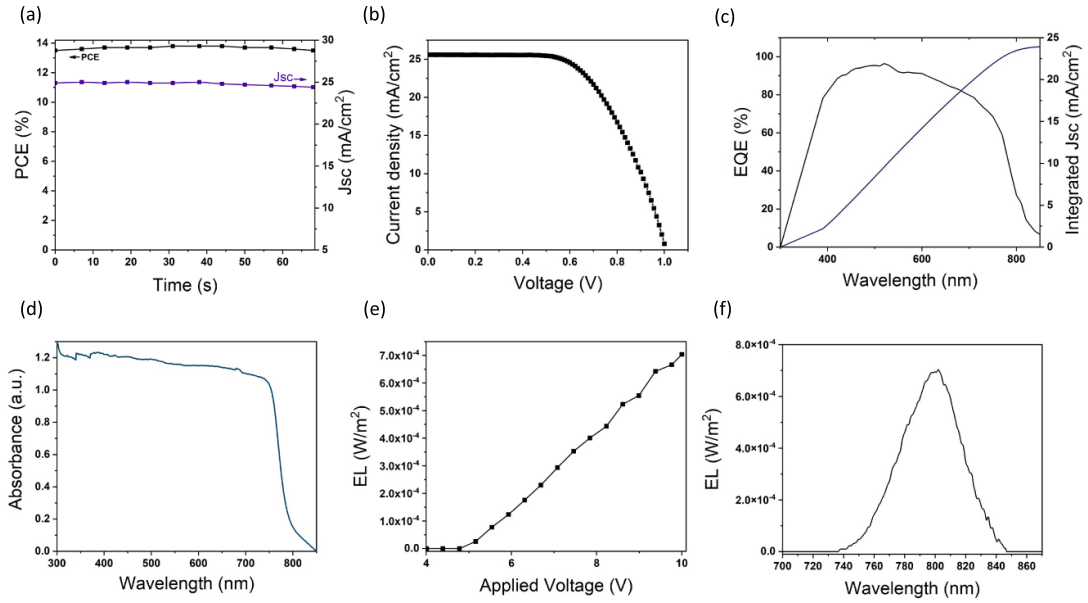

Figure 2. (a) Stability power output and J_{sc} of the ITO-PSC as a function of time. (b) *J–V* curve and (c) EQE curve of the champion ITO-PSC with PCE of 15.3%, $J_{sc} = 25.6$ mA cm^{-2}, FF = 59% and V_{oc} of 1.00 V. (d) Absorbance spectrum of the $FA_{0.85}MA_{0.15}Pb(I_{0.85}Br_{0.15})_3$ composition. (e) Electroluminescence (EL) measurement of the ITO-PSCs as a function of the applied voltage. (f) EL spectra of the ITO-PSCs when functioning as a light-emitting diode (LED).

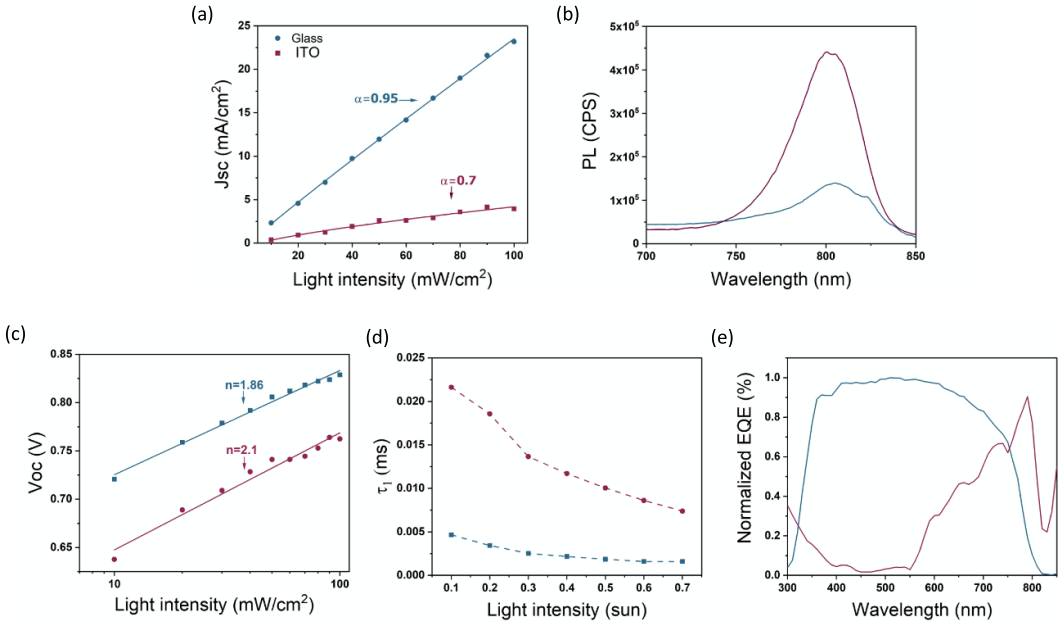

Figure 3. (a) J_{sc} dependence on the light intensity for illumination from both sides of the cell. (b) PL measurement of the cell from both sides. (c) V_{oc} dependence on the light intensity for illumination from both sides of the cell. (d) Recombination electron lifetime, extracted from intensity modulated photo-voltage spectroscopy (IMVS) measurement. (e) EQE curve of illumination from both sides of the cell.

Due to the fact that in open-circuit conditions the current is zero, and the rate of recombination is equal to the rate of charge injection, this dependence can provide information regarding the recombination process in the cell and its dominant mechanism [16, 18]. The dependence of V_{oc} on the light intensity is according to $V_{oc} \propto \left(n_{id}kTq^{-1}\right)\ln(I)$, when n_{id} is the ideality factor, k is the Boltzmann's constant, T is the temperature and q is the elementary charge. When plotting the V_{oc} dependence on a semi-logarithmic graph, the ideality factor can be extracted from the slope.

For the glass-side illumination, the value of the ideality factor is 1.86, indicating that the main recombination mechanism is Shockley–Read–Hall recombination in the bulk, via bulk defects [18]. In the case of the ITO-side illumination, the value of the ideality factor is 2.1, which is attributed to recombination

in multiple traps and intergap defect distribution. This is in good agreement with the value of α, and can explain the poor current density and efficiency of the ITO-side measurements.

In order to observe more information on the electron recombination process in the ITO-PSCs, an IMVS measurement was performed on both sides of the cell. In the IMVS measurement, modulated light irradiates the cell at different light intensities. The generated voltage is measured and provides information about the lifetime of the electrons in the solar cell. For each measurement, the output data are two semi-circles (figure S1). Each one relates to a different layer or interface of the solar cell's structure [19]. Using these semicircles, the relevant time constants can be extracted according to $\tau = 1/\omega_{\min}$, when $\omega_{\min}$ is the frequency of the minimum point of the semi-circle. The low-frequency semi-circle is related to the electron lifetime in the TiO_2 layer. In this region, no significant difference was observed between the glass-side and the ITO-side measurements, and the lifetimes were at the same order of magnitude (figure S2). The high-frequency region is attributed to the electron lifetime at the perovskite/TiO_2 interface [20]. As can be seen in figure 3(d), for the measurements of both sides, the lifetime decreases with the increase in the light intensity. This is due to the enhanced photon flux, which results in a larger electron density that increases the probability of recombination. The recombination lifetime is longer for the ITO-side measurement than for the glass-side measurement, by one order of magnitude for all light intensities. This can be explained by the distance between the location of the electron-generation and the perovskite/TiO_2 interface. Upon illuminating the cell from the ITO-side, the photons are absorbed in the perovskite located inside the mp-ITO layer. Therefore, the generated electrons travel a long distance (a few micrometers) until they are injected into the TiO_2 and are more likely to get caught in multiple trap states (as was observed by the ideality factor) [21]. This explains the longer recombination lifetime at the perovskite/TiO_2 interface for the ITO-side measurement. In addition, the long recombination lifetime at the interface of the ITO side explains the high FF in the ITO-side current–voltage measurements [22].

The normalized EQE of both sides (figure 3(e)) provides more information about the charge transport in the device. While the EQE of the glass- side shows a typical shape for an HTL free cell, the highest EQE values for the ITO-side illumination are in the long wavelength region of 600–800 nm. As previously reported, the EQE in the long-wavelength region is related to the functionality of the HTL [23, 24]. It can be assumed that the relatively high EQE values in this region are due to the charge transport in the ITO layer. This suggests that the main contribution to the performance comes from the ITO side, while not all the electrons reach the TiO_2 electrode.

Electrochemical impedance spectroscopy (EIS) measurements were performed on the ITO-PSC in the dark and under illumination from both sides. Figure S3 presents the Nyquist plot of the EIS measurements in the dark, in a voltage range of 0.1–0.8 V. Two clear semi-circles can be observed in figures S3(a) and S7(b) in orthonormal Nyquist plot. Therefore, the data were fitted to an equivalent circuit containing two *R*–*C* elements, as shown in figure S3(b). All capacitance elements were replaced with constant phase elements (CPEs) to fit the realistic system [25]. The resistance in the high-frequency region (figure S3(c)) is related to the charge transfer resistance at the ITO/perovskite interface, while the low-frequency resistance (figure S3(d)) is attributed to the TiO_2/perovskite interface [26, 27].

EIS measurements under illumination of 70 mW cm^{-2} were performed on both sides of the solar cell. Figure 4(a) presents the Nyquist plot for the ITO side, which is composed of four semi-circles, as well as four peaks in the Bode phase plot (figure S4), and the Nyquist plot for the glass side, which shows only three semi-circles, orthonormal Nyquist plots are presented in figure S7(a). The data from the EIS were fitted based on the equivalent circuits, as presented in figures S5(a) and S5(b). The semi-circle in the high-frequency region is usually attributed to the charge transfer resistance ($R_{ct\text{-}1}$) at the perovskite/ITO interface. The second semi-circle, in the intermediate frequency domain, is the charge transfer resistance in the perovskite layer ($R_{ct\text{-}2}$). Although in this structure there is no separate perovskite layer, the perovskite in the spacer layer can be considered as the active layer, and it has its own resistance and capacitance [14, 28–31].

The next semi-circle is related to the charge recombination resistance at the perovskite/TiO_2 interface (R_{rec}). The electron transfer at this interface is fast. Therefore, it is not likely to observe its resistance in the EIS spectra. The additional semicircle that only appears in the ITO-side measurement in the low-frequency region can be attributed to the ion diffusion in the solar cell [32]. Generally, the ion diffusion is slower compared to the electron transfer. Therefore, it usually cannot be observed in EIS measurements. In this case, when illuminating from the ITO side, the electrons are generated far from the photo-anode, which makes the ion migration more significant.

Figure 4(b) presents the series resistance of the ITO-PSC, measured from both sides. Surprisingly, although the structure is identical in both measurements, the R_s values are different. The reason is that the series resistance is composed of the resistance of the layers, the contacts, and the internal resistance of the layers. Therefore, the higher R_s values measured for the ITO-side measurement indicate that the internal resistances are higher in the case of ITO-side illumination. This is in good agreement with the PV results.

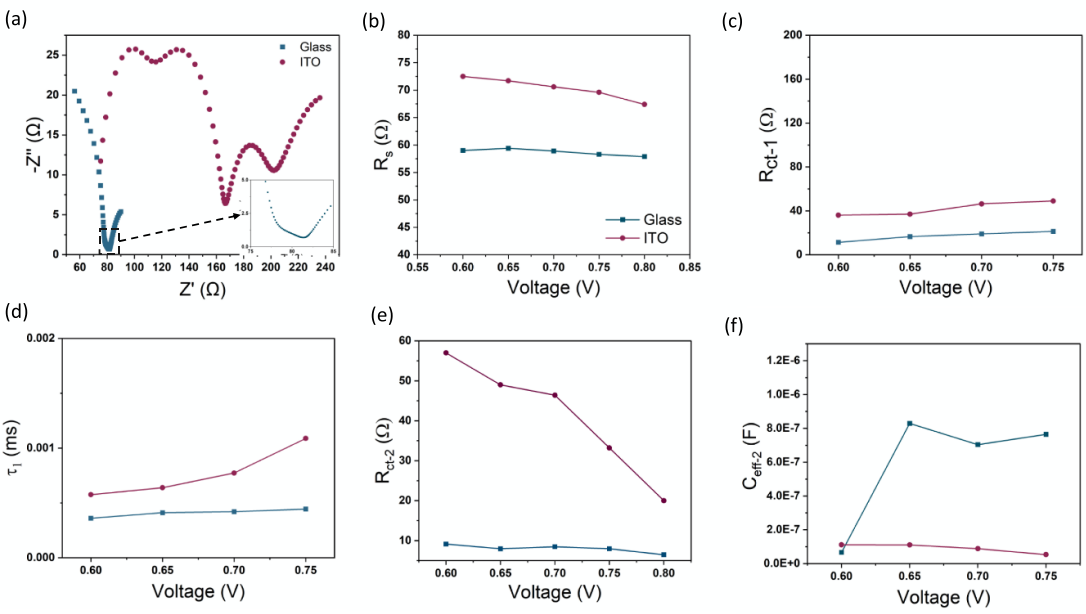

Figure 4. EIS measurement for both sides of the cell. (a) Nyquist plot for glass- and ITO-side measurements, for 0.65 V bias under illumination. Inset: enlargement of the second semi-circle. (b) Series resistance for measurements of both sides. (c) Charge transfer resistance at the perovskite/ITO interface. (d) Transport time at the perovskite/ITO interface. (e) Charge transfer resistance in the perovskite. (f) Effective capacitance in the perovskite layer.

As can be seen in figure 4(c), the charge transport resistance at the perovskite/ITO interface is slightly higher when illuminating the ITO side. Moreover, the transport time at this interface, calculated by the capacitance multiplied by the resistance (figure 4(d)), shows that the illumination from the glass-side is more efficient for the charge transport than the illumination from the ITO side. It can also be concluded that this interface (perovskite/ITO) is not sensitive to the applied voltage. The resistance for both sides barely changes with the applied voltage range.

The resistance in the perovskite layer, $R_{ct\text{-}2}$, is decreasing with the applied voltage, as presented in figure 4(e). When illuminating from the ITO side, the resistance is much higher than in the case of illumination from the glass side, which supports the higher PV performance of the cells when measured from the glass side.

Another parameter that can be extracted from the EIS fitting is the effective capacitance, which displays the electron density in our material. In EIS measurements, the capacitance element is often replaced with CPE, which models the behavior of an imperfect capacitor. Due to the mesoscopic structure, the inhomogeneous surface of the electrode results in distribution of the current density. In this case, the phase angle of the impedance is independent of frequency, and the ideal capacitance is not accurate. The CPE is defined by $Z_{\mathrm{CPE}} = R/(1 + Y_0\, R(j\omega)^n)$, where Y_0 represents the capacitance information, ω is the angular frequency, R is the parallel resistance in the circuit and n is an empirical constant between 0 and 1. The closer n is to 1, the closer the CPE is to an ideal capacitor. The effective capacitance can be calculated using the CPE parameters Y_0 and n [25, 33].

The effective capacitance, presented in figure 4(f), shows that the capacitance in the perovskite layer is higher in the case of illumination from the glass side compared to the case of illumination from the ITO side. This supports a higher current density for the cells illuminated from the glass side.

2.2. Bifacial configuration

As stated earlier, one of the unique features of this solar cell structure is its possibility to be measured in a bifacial configuration without the need for an additional layer or device. There is no consensus regarding bifacial solar cell efficiency. A commonly used term is 'equivalent efficiency', which is equal to the efficiency of the monofacial SC, which is able to produce the same power density under the same test conditions [7]. The equivalent efficiency can be calculated using the following equation:

$$\mathrm{Eff_{Bi}} = \mathrm{Eff_{glass}} + R_{\mathrm{A}} \times \mathrm{Eff_{ITO}}. \tag{1}$$

When R_{A} is the albedo, part of the light is reflected back to the backside of the cell. Calculating the equivalent efficiency does not require measurements in bifacial configuration, only separate measurements

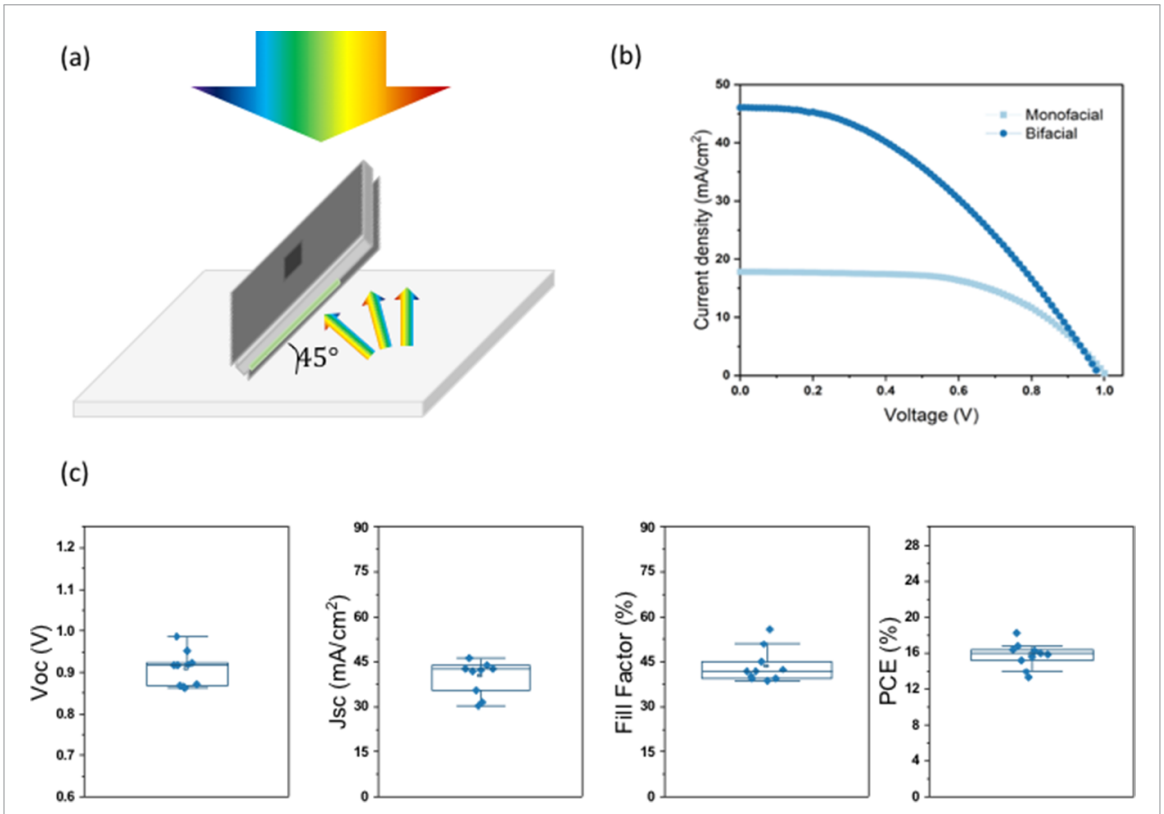

Figure 5. (a) Illustration of the solar simulator measurement in a bifacial configuration of the cell. The cell, covered with 0.1 cm^2 mask from both sides, is held at 45° under 1 sun illumination. Testing stage, covered with white paper, reflects some of the light back to the backside of the cell. (b) *J–V* curve of the champion bifacial solar cell measured after being kept overnight in a nitrogen glove box. (c) PV parameters of the bifacial configuration measurements.

for each side of the cell. However, there are no calculations for the J_{sc}, V_{oc} and FF of the bifacial configuration. Therefore, measuring the cell using a reflective object enables us to test the true performance of the ITO-PSCs in a bifacial configuration. The measurements were conducted under 1 sun illumination, where the measurement stage was covered by a white paper, with 60% albedo [11]. As illustrated in figure 5(a), the cell was held at 45° from the stage, and covered from both sides with masks, leaving only 0.1 cm^2 active area from each side. Our suggested electron–hole generation and transport mechanism in the case of the bifacial illumination can be seen in figure S8.

Figure 5(c) presents the various PV results of the ITO-PSCs. As can be seen in the figure, the current density has improved by 66% compared to the monofacial cells. This is expected to be due to the dependence of J_{sc} on the light intensity, as discussed above. Clearly, the bifacial configuration results in more light irritation in the cell and therefore enhanced current density. The average efficiency, strongly influenced by the current, increased to 16%. The champion bifacial cell achieved 18.3% PCE, with a current density of 46 mA cm^{-2} (figure 5(b)). The FF slightly decreased, due to higher series resistance [34].

The stability of the un-encapsulated devices was tested as well, in ambient conditions and under illumination. The experiments were carried out on 15 cells. As presented in figure S6(a), after 60 days in ambient conditions, the cells preserved 90% of their initial efficiency. Figure S6(b) presents their stability under continuous illumination in a nitrogen glove box, in which 92% of the initial efficiency was preserved after 90 hours of illumination.

3. Conclusion

Here, we demonstrate triple oxide screen-printed mp layers where the perovskite penetrates the pores and does not form a separate layer between the selective contacts. These cells were measured from both sides due to their transparent contact. The glass side shows better PV results than the ITO side, where it was revealed that the recombination mechanism depends on the illumination side. EIS measurements support the PV results from illumination of both sides, detecting higher charge transport resistance in the perovskite when illuminating from the ITO side, caused by multiple trap distributions. The EQE of the cells measured on both sides clearly shows the role of hole transport material. It can be assumed that the thickness of the layers, especially the mp-ITO layer, has a significant influence on the gap between the performance of the glass side

and the ITO side. Thinner layers may decrease the glass-side performance but will reduce the traveling distance of the electrons to the electrode when illuminating the ITO side. Therefore, the ITO-side performance is expected to improve. Interestingly, this triple oxide mp layer solar cell structure shows EL response when functioning as an LED device. Finally, we demonstrate the ability to use this solar cell in a bifacial configuration using a highly reflective background, which results in an increase in the efficiency, demonstrating 18.3% efficiency.

4. Experimental section

4.1. Materials and solvents

Hellmanex III detergent, Ti diisopropoxide bis(acetylacetonate) (75% weight [wt.], in isopropanol), polyvinylpyrrolidone (PVP, 55 K and 10 K), terpineol, PbI2 (99%), N,N-dimethylformamide (anhydrous 99.8%) and isopropyl alcohol (anhydrous 99.5%) were purchased from Sigma-Aldrich. MAI and FAI were purchased from GreatCell Solar. Titanium(IV) chloride was purchased from Wako. Ethanol absolute (99.5%) and extra dry dimethyl sulfoxide (99.7%) were purchased from Acros. ITO (nanopowder <50 nm particle size) was purchased from Alpha Aesar. Zr-Nanoxide and TiO_2 pastes were purchased from Wonder Solar. Acetic acid was purchased from Bio-Lab. All the materials were used as received.

4.2. Preparation of ITO nanoparticle paste

PVP solution (20% wt.) was prepared by dissolving equal weights of two PVPs of different viscosities (10 and 55 K) in ethanol. One gram of ITO nanopowder was dispersed in a mixture of 8.9 ml ethanol, 830 μl triple distilled water (TDW) and 166 μl acetic acid. After 50 half-second pulses of a sonic horn and 45 min stirring, 0.9 g of ethanol was added, following by 10 min stirring. Next, 1.7 g of the PVP solution was added, and the dispersion was stirred for 1 h. Finally, the mixture was evaporated in a rotary evaporator for about 20 min.

4.3. mp-ITO scaffold slide preparation

The slides were prepared by the procedure reported in the past [13, 35]. In brief, FTO-coated slides were etched with a laser to segregate anodal and cathodal areas. The slides were washed and put in an ultrasonic bath (20 min in soap, 15 min in Hellmanex detergent (1% in water) and 20 min in an ethanol (15%), acetone (15%) and water (70%) mixture). The substrates then underwent oxygen plasma treatment for 10 min. The hole blocking layer was fabricated by spin coating the FTO-coated slides with an 11.8% diisopropoxide bis(acetylacetonate) solution in ethanol (5000 rpm, 30 s), then annealed on a hot plate for 30 min in 450 °C.

Next, the slides were treated with a $TiCl_4$ solution (1.6 ml $TiCl_4$ in 150 ml TDW) and put in an oven for 30 min (70 °C), then rinsed in water and annealed on a hot plate for 30 min in 450 °C, with slow heating.

The TiO_2 paste (2:1%wt. diluted with ethanol) was screen printed on the slides using a 120 mesh and sintered on a hot plate for 30 min at 500 °C. Then, a second $TiCl_4$ was used, identical to the one described above.

The ZrO_2 layer was screen printed using a ZrO_2 paste (6:1%wt. diluted with ethanol) and a 120 mesh and sintered on a hot plate for 30 min at 500 °C.

Finally, the ITO paste was screen printed with a 32 mesh and sintered in an oven for 90 min at 600 °C.

4.4. Perovskite solution preparation and deposition

PbI_2 and $PbBr_2$ (85% and 15%, respectively) solutions were prepared (1.6 M, 0.5 ml), with 25:75 dimethyl sulfoxide:N,N-dimethylmethanamide (DMSO:DMF) solvent ratio. The substrates were heated to 70 °C on a hot plate inside a nitrogen glove box, while 2 μl of the solution was drop cast onto them and annealed at 70 °C for 30–45 min. The substrates were then immersed for 30 min in a 15:85 MABr:FAI solution in isopropanol (0.06 M, 10 ml), followed by dipping in clean isopropanol and annealing on a hot plate for 120 min at 70 °C.

4.5. PV characterization

Current–voltage measurements were performed using a solar simulator system (Oriel *I–V* test station, Sol3A simulator with a 450 W Xe lamp and output power of air mass coefficient 1.5 global sunlight). *J–V* curves were obtained by applying a varying external bias from 1 to −0.1 V on the cell, and measuring the photocurrent with a Keithley model 2400 digital source meter. The measurements were carried out after 20 s exposure to 1 sun light, with voltage steps and dwell times of 10 mV and 40 ms, respectively. The PV performance was measured over an active area of 0.1 cm^2.

EQE measurements were conducted using the Fast EQE system from Quantum Zurich (Switzerland). The solar cell was illuminated, with a spot 4 mm in diameter, by 35 LEDs, whose wavelengths lie in a range from 390–1080 nm. A reference photodiode was used to measure the number of photons arriving in the solar

cell. The total short-circuit current density (J_{sc}) was calculated from the EQE data by using the spectral irradiance of AM1.5G spectrum at 1 sun solar intensity.

5. IMVS and EIS measurements

The IMVS and EIS were measured using an Autolab Potentiostat-Galvanostat (PGSTAT) with a FRA32M LED driver equipped with a cool white light source. A Nova 1.1 software program was used to collect and analyze the obtained data. The IMVS measurements were obtained by illuminating the sample at different light intensities, varying from 0.1–0.7 sun, with a sinusoidal wave modulation, with frequencies ranging from 1 Hz–50 kHz. The EIS measurements were conducted at different bias voltages with perturbation of 10 mV from 1 MHz–0.1 Hz, under dark conditions, and under 70 mW cm^{-2} illumination.

6. Optical characterizations

The absorbance measurements were conducted using a Jasco V-670 ultraviolet (UV) –Vis near infrared (NIR) spectrophotometer. The PL measurements were performed using a Horiba Fluoromax-4 spectrofluorometer. The device operates with a 150 W continuous wave (CW) ozone-free xenon arc lamp. An excitation grating of 1200 groove mm^{-1} blazed at 330 nm. An emission grating of 1200 groove mm^{-1} blazed at 500 nm with a photomultiplier detector.

7. EL measurements

EL measurements were performed using an F1000-VISNIR optic fiber with a cosine receptor, and a StellarNet BLACK-Comet Spectrometer with a CRX-100 partially depleted absorber photodetector. *I–V* curve measurements were performed using the Keithley model 2400 digital source meter.

Data availability statement

All data that support the findings of this study are included within the article (and any supplementary files).

Acknowledgments

We would like to thank the Israel ministry of energy and the Israel ministry of science for their financial support in this project.

ORCID iD

Lioz Etgar https://orcid.org/0000-0001-6158-8520

References

[1] Photovoltaic research *Best Research-Cell Efficiency Chart* NREL (available at: www.nrel.gov/pv/cell-efficiency.html)
[2] Ponseca C S *et al* 2014 Organometal halide perovskite solar cell materials rationalized: ultrafast charge generation, high and microsecond-long balanced mobilities, and slow recombination *J. Am. Chem. Soc.* **136** 5189–92
[3] Yang W S, Noh J H, Jeon N J, Kim Y C, Ryu S, Seo J and Seok S il 2015 High-performance photovoltaic perovskite layers fabricated through intramolecular exchange *Science* **348** 1234–7
[4] Eperon G E, Stranks S D, Menelaou C, Johnston M B, Herz L M and Snaith H J 2014 Formamidinium lead trihalide: a broadly tunable perovskite for efficient planar heterojunction solar cells *Energy Environ. Sci.* **7** 982–8
[5] Noh J H, Im S H, Heo J H, Mandal T N and Seok S il 2013 Chemical management for colorful, efficient, and stable inorganic-organic hybrid nanostructured solar cells *Nano Lett.* **13** 1764–9
[6] Stranks S D, Eperon G E, Grancini G, Menelaou C, Alcocer M J P, Leijtens T, Herz L M, Petrozza A and Snaith H J 2013 Electron-hole diffusion lengths exceeding 1 micrometer in an organometal trihalide perovskite absorber *Science* **342** 341–4
[7] Guerrero-Lemus R, Vega R, Kim T, Kimm A and Shephard L E 2016 Bifacial solar photovoltaics—a technology review *Renew. Sust. Energ. Rev.* **60** 1533–49
[8] Pang S *et al* 2018 Efficient bifacial semitransparent perovskite solar cells using Ag/V_2O_5 as transparent anodes *ACS Appl. Mater. Interfaces* **10** 12731–9
[9] Pang S *et al* 2017 Efficient bifacial semitransparent perovskite solar cells with silver thin film electrode *Sol. Energy Mater. Sol. Cells* **170** 278–86
[10] Hanmandlu C, Chen C Y, Boopathi K M, Lin H W, Lai C S and Chu C W 2017 Bifacial perovskite solar cells featuring semitransparent electrodes *ACS Appl. Mater. Interfaces* **9** 32635–42
[11] Gao L, Zhao E, Yang S, Wang L, Li Y, Zhao Y and Ma T 2017 Light engineering for bifacial transparent perovskite solar cells with high performance *Opt. Eng.* **56** 1
[12] Rong Y, Hu Y, Mei A, Tan H, Saidaminov M I, Seok S, McGehee M D, Sargent E H and Han H 2018 Challenges for commercializing perovskite solar cells *Science* **361** eaat8235

[13] Schneider A, Efrati A, Alon S, Sohmer M and Etgar L 2020 Green energy by recoverable triple-oxide mesostructured perovskite photovoltaics *Proc. Natl Acad. Sci.* **117** 31010–7
[14] Liu T, Liu L, Hu M, Yang Y, Zhang L, Mei A and Han H 2015 Critical parameters in TiO_2/ZrO_2/carbon-based mesoscopic perovskite solar cell *J. Power Sources* **293** 533–8
[15] Rühle S 2016 Tabulated values of the Shockley-Queisser limit for single junction solar cells *Sol. Energy* **130** 139–47
[16] Singh T and Miyasaka T 2018 Stabilizing the efficiency beyond 20% with a mixed cation perovskite solar cell fabricated in ambient air under controlled humidity *Adv. Energy Mater.* **8** 1700677
[17] Lv S *et al* 2014 Mesoscopic TiO_2/$CH_3NH_3PbI_3$ perovskite solar cells with new hole-transporting materials containing butadiene derivatives *Chem. Commun.* **50** 6931–4
[18] Tress W, Yavari M, Domanski K, Yadav P, Niesen B, Correa Baena J P, Hagfeldt A and Graetzel M 2018 Interpretation and evolution of open-circuit voltage, recombination, ideality factor and subgap defect states during reversible light-soaking and irreversible degradation of perovskite solar cells *Energy Environ. Sci.* **11** 151–65
[19] Guillén E, Ramos F J, Anta J A and Ahmad S 2014 Elucidating transport-recombination mechanisms in perovskite solar cells by small-perturbation techniques *J. Phys. Chem.* C **118** 22913–22
[20] Avigad E and Etgar L 2018 Studying the effect of MoO_3 in hole-conductor-free perovskite solar cells *ACS Energy Lett.* **3** 2240–5
[21] Hsiao P T, Tung Y L and Teng H 2010 Electron transport patterns in TiO_2 nanocrystalline films of dye-sensitized solar cells *J. Phys. Chem.* C **114** 6762–9
[22] Reusch M, Bivour M, Hermle M and Glunz S W 2013 Fill factor limitation of silicon heterojunction solar cells by junction recombination *Energy Proc.* **38** 297–304
[23] Tressl W, Marinoval N, Inganas O, Nazeeruddin M K, Zakeeruddinl S M and Graetzell M 2014 The role of the hole-transport layer in perovskite solar cells-reducing recombination and increasing absorption *2014 IEEE 40th Photovoltaic Specialist Conf. (PVSC)* pp 1563–6
[24] Marinova N, Tress W, Humphry-Baker R, Dar M I, Bojinov V, Zakeeruddin S M, Nazeeruddin M K and Grätzel M 2015 Light harvesting and charge recombination in $CH_3NH_3PbI_3$ perovskite solar cells studied by hole transport layer thickness variation *ACS Nano* **9** 4200–9
[25] Chang B Y 2020 Conversion of a constant phase element to an equivalent capacitor *J. Electrochem. Sci. Technol.* **11** 318–21
[26] Zhang J, Meng Z, Guo D, Zou H, Yu J and Fan K 2018 Hole-conductor-free perovskite solar cells prepared with carbon counter electrode *Appl. Surf. Sci.* **430** 531–8
[27] Rong Y, Ku Z, Mei A, Liu T, Xu M, Ko S, Li X and Han H 2014 Hole-conductor-free mesoscopic TiO_2/$CH_3NH_3PbI_3$ heterojunction solar cells based on anatase nanosheets and carbon counter electrodes *J. Phys. Chem. Lett.* **5** 2160–4
[28] Behrouznejad F, Tsai C M, Narra S, Diau E W G and Taghavinia N 2017 Interfacial investigation on printable carbon-based mesoscopic perovskite solar cells with NiO_x/C back electrode *ACS Appl. Mater. Interfaces* **9** 25204–15
[29] Xu X, Liu Z, Zuo Z, Zhang M, Zhao Z, Shen Y, Zhou H, Chen Q, Yang Y and Wang M 2015 Hole selective NiO contact for efficient perovskite solar cells with carbon electrode *Nano Lett.* **15** 2402–8
[30] Bashir A *et al* 2018 Spinel Co_3O_4 nanomaterials for efficient and stable large area carbon-based printed perovskite solar cells *Nanoscale* **10** 2341–50
[31] Ahmad Z, Mishra A, Abdulrahim S M and Touati F 2020 Electrical equivalent circuit (EEC) based impedance spectroscopy analysis of HTM free perovskite solar cells *J. Electroanal. Chem.* **871** 114294
[32] Bag M, Renna L A, Adhikari R Y, Karak S, Liu F, Lahti P M, Russell T P, Tuominen M T and Venkataraman D 2015 Kinetics of ion transport in perovskite active layers and its implications for active layer stability *J. Am. Chem. Soc.* **137** 13130–7
[33] Brug G J, van den Eeden A L, Sluyters-rehbach M and Sluyters J H 1984 The analysis of electrode impedances complicated by the presence of a constant phase element *J. Electroanal. Chem.* **176** 275–95
[34] Russell T C R, Saive R, Augusto A, Bowden S G and Atwater H A 2017 The influence of spectral albedo on bifacial solar cells: a theoretical and experimental study *IEEE J. Photovolt.* **7** 1611–8
[35] Schneider A, Alon S and Etgar L 2019 Evolution of photovoltaic performance in fully printable mesoscopic carbon-based perovskite solar cells *Energy Technol.* **7** 1900481